Cancer Nanotechnology

RESEARCH

Open Access

As1411-modified liposomes to enhance drug utilization and augment the anti-tumor efficacy

Danhuan Zhang[1,2], Lingyun Chen[3], Yang Zhao[4], Hao Ni[1], Qiuying Quan[1], Jun Ma[2*] and Lingchuan Guo[1*]

*Correspondence:
drma258@163.com;
jjok33202@126.com

[1] Department of Pathology,
The First Affiliated Hospital
of Soochow University,
Suzhou 215006, Jiangsu, China
[2] Department of Nephrology,
Tongren Hospital, Shanghai
Jiaotong University School
of Medicine, Shanghai 200336,
China
[3] Shanghai Electric Power
Hospital, Shanghai, China
[4] Center of Clinic Oncology, The
Affiliated Hospital of Xuzhou
Medical University, Xuzhou,
China

Abstract

Background: The utilization of liposomes in drug delivery has garnered significant attention due to their efficient drug loading capacity and excellent biocompatibility, rendering them a promising platform for tumor therapy. However, the average size of liposomes ~ 100 nm leads to liposomes being susceptible to hepatic and renal metabolism to excretion outside the body leading to poor drug delivery efficiency with a total utilization rate of less than 0.7%, resulting in unfavorable treatment outcomes.

Results: We have developed a novel liposome platform equipped with tumor surface nucleolin-targeting capacity to enhance drug accumulation at the tumor in vivo. The encapsulation of doxorubicin through thin film hydration has resulted in the formation of D@L-AS1411. Through in vivo experiments, we have demonstrated the effective accumulation of D@L-AS1411 at the tumor site and its ability to improve doxorubicin utilization rates by 40%. Additionally, D@L-AS1411 induces immunogenic death of tumor cells, release of tumor-associated antigens, upregulation of calreticulin expression, and recruitment of active T cell infiltration, and ultimately improves the therapeutic efficacy against tumors (70%).

Conclusions: Based on the nucleic acid aptamer AS1411, D@L-1411 is developed to specifically enhance the accumulation of Dox at tumor sites, thereby inhibiting and enhancing the anti-tumor effect. In summary, this study not only provides an efficient tumor-targeting delivery platform but also contributes to the improvement of chemotherapy–immunotherapy combination for tumor treatment strategy in the clinic.

Keywords: Liposome, AS1411, Immunogenic death, Targeted delivery

Introduction

Recently, the development of safe and effective drug delivery vehicles has been an urgent requirement in the treatment of tumors. Traditional small molecule anti-tumor drugs can effectively inhibit tumor cell growth and induce tumor cell apoptosis to eliminate tumors (Yang and Nguyen 2021). However, long-term drug administration inevitably gives rise to the gradual development of drug resistance in tumor cells,

ultimately leading to suboptimal treatment outcomes (Law 1956). Additionally, the toxic side effects of these small molecule drugs limit the maximum dose that can be administered, ultimately leading to drug failure in the area of cancer therapy (Zhang et al. 2023; Wendler et al. 2021). To address this issue, several drug delivery vehicles, including liposomes (Chen et al. 2014; Liu et al. 2019), mesoporous silica (Wang et al. 2018; Si et al. 2024), albumin manganese dioxide (Liu et al. 2012; Jiang et al. 2024), and micelles (Imran ul-haq et al. 2013; Li et al. 2020) have been developed and widely utilized in the tumor treatment field. These novel vehicles can improve drug properties and accumulate drugs at the tumor site through the permeation and retention (EPR) effect (Al-Harbi et al. 2020; Pavitra et al. 2021; Kalyanaraman et al. 2019; Wang et al. 2023). However, the overall drug utilization rate remains low due to the readily capture of nanoparticles by the liver's vascular reticular system and their subsequent excretion through the kidneys (Sugarbaker and Stuart 2021). Therefore, there continues to be an urgent need for enhancing drug accumulation at the tumor site.

Liposomes are primarily composed of lecithin, cholesterol, and polyethylene glycol, exhibiting a cell-like membrane spherical structure with a size distribution of ~ 50–1000 nm (Chen et al. 2014; Xu et al. 2021). Due to the presence of hydrophilic cores and hydrophobic phospholipid bilayers, liposomes can specifically encapsulate hydrophilic and hydrophobic drugs within their respective core and layers to facilitate drug loading (Pavitra et al. 2021). Nevertheless, their particle size of ~ 100 nm makes them susceptible to being captured by the liver's vascular network system, thereby reducing drug enhancement and utilization. In response, various Liposome nanoparticles that respond to the tumor microenvironment have been developed, including pH (Ibrahim et al. 2014; Lokova and Zaborova 2019) and temperature-responsive nano-systems (Fu et al. 2019; Bing et al. 2018), that release drugs according to the tumor microenvironment, effectively mitigating premature drug release, leakage, and related issues. Although these designs reduce toxic drug side effects, the overall utilization rate remains low.

One promising approach involves utilizing the aptamer AS1411 (Yazdian-Robati et al. 2020), a 25-base DNA sequence that targets nucleolins on the surface of tumor cells (Jiang et al. 2020; Kong et al. 2019; Pesarrodona et al. 2020). Compared with other target-modified nanoparticles, such as antibodies and proteins, AS1411 smaller size enables better modification on the surface of nanocarriers without affecting nanoparticle properties, making it a valuable asset in tumor treatment.

In this regard, we encapsulated Dox within liposome nanoparticles through a two-step reaction, successfully attaching AS1411 on the surface of liposome to enhance the tumor-targeting ability and improve Dox accumulation at the tumor site. Studies reveal that Dox induces immunogenic cell death (ICD) and stimulates calreticulin (CRT) expression in tumor cells, thereby eliciting an immune response. Upon tail vein injection of this nanodrug, AS1411 recognizes tumor cells, increasing nanoparticle accumulation at the tumor site, and facilitating cell uptake. After uptake by tumor cells, Dox is released, inducing cancer cell apoptosis and stimulating CRT expression, which is recognized as an antigen signal by the immune system, activating T lymphocyte activity and enhancing the anti-tumor effect. These findings demonstrate that

AS1411 lipid nanoparticles serve as an effective drug delivery platform for achieving chemotherapy immunity combined with anti-tumor therapeutic outcomes.

Materials and methods

All the chemical reagents were purchased from Sigma unless otherwise specified. Dox was obtained from Sheng Gong (shanghai, China). AS1411-PEG$_{2000}$-DSPE were obtained from PONSURE Biological Company (shanghai, China). DMEM medium and FBS were purchased from GIBCO-RBL (Grand Island, NY, USA). All antibodies were acquired from Abcome (Shanghai, China). All biochemical reagents were used without further purification.

Cells and animals

Murine colon cancer cells RENCA were obtained from the First Affiliated Hospital of Soochow University (Suzhou, China). RENCA cells were cultured in 1640 medium containing 10% fetal bovine serum (FBS) and 1% penicillin/streptomycin at 37 °C under 5% CO_2 in a cell incubator (Thermal Fisher Inc, USA).

Balb/c female mice (5–6 weeks old, 20 g) were purchased from the animal experimental center of East Hospital of Shanghai (Shanghai, China). All procedures strictly complied with the ethical and legal requirements under the Administration Committee of Experimental Animals in Shanghai and were approved by the Ethics Committee of Tongren Hospital of Shanghai Jiaotong University School of Medicine.

Synthesis and characterization of D@L-AS1411

D@L-AS1411 was prepared by the thin film hydration method (Xiong et al. 2021). Briefly, 220 mg (0.47 mol) lecithin of soybean and 118 mg (0.3 mol) of cholesterol were added with 10 ml trichloromethane into the flask. Subsequently, the solution was evaporated by a rotary evaporator to form a lipid film on the flask. Next, 5 ml PBS containing 2 mg Dox was added into the flask and sonicated in a water bath for 30 min. Following this, 3.5 mg (0.011 mol) of AS1411-PEG$_{2000}$-DSPE was added to the mixture and vortexed for 1 min. The solution was then extruded 20 times using a liposome extruder equipped with 200 nm polycarbonate membrane filters. The free Doxs were isolated by ultrafiltration device (Amicon Ultra-15) with 30 kDa ultrafiltration membranes. The sample was stored at 4 °C.

The morphology of liposomes was observed by transmission electron microscopy. The size distribution and zeta potential of D@L-AS1411 were analyzed by Mastersizer (ZEN3600, UK). The loading of Dox and AS1411 were detected though UV–Vis and characteristic absorption at 480 nm and 260 nm, respectively.

The stability and drug release behavior of D@L-AS1411

The stability of D@L-AS1411 was detected at PBS buffer, FBS (5%) buffer and Triton X-100 (10%), respectively. Briefly, 100 μl D@L-AS1411 was dissolved, respectively, into this buffer and stirred at room temperature. At 0, 2, 6, 12, 24, and 72 h, the buffer (1 ml) was taken out for analysis by Mastersizer.

Dox release behavior from D@L-AS1411 was detected at room temperature by a dialysis bag (molecular weight cutoff, 3.5 kDa). 5 ml of D@L-AS1411 was added to the

dialysis bag and immersed into 25 ml PBS and under shaking at 200 rpm to detect Dox released. The buffer (1 ml) was taken out and analyzed by UV–Vis at 480 nm. After this, 1 ml PBS was added to the 24 ml PBS to keep a consistent volume for 25 ml. Finally, the accumulated total release of Dox was detected by the standard curve.

Cellular uptake of D@L and D@L-AS1411

The intracellular uptake of D@L-AS1411 was assessed by confocal laser scanning microscope (CLSM) (Nikon, Japan) and flow cytometry. 10^6 RENCA tumor cells were seeded in 12 mm^2 glass-bottom for 12 h. Free AS1411 (0 nm, 2 nm, 10 nm, and 20 nm) were added to the medium and incubated for 2 h, respectively. After that, a fresh medium containing D@L-AS1411 with a concentration of Dox 2 μM for the other 6 h. Finally, cells were washed with PBS for 3rd and DAPI was used to stain for 10 min at 4 ℃. The fluorescence signal was obtained by CLSM. Similarly, we analyzed the effectiveness of cellular uptake by flow cytometry with excitation lasers of 488 nm.

CRT expression on the tumor cell membrane

10^6 RENCA tumor cells were seeded in 12 mm^2 glass-bottom for 12 h. The cells were further incubated with a free medium containing D@L-AS1411 (Dox concentration: 5 μM) for the other 6 h. Afterward, the cells were washed with PBS 3 times and incubated with PE conjugate CRT-antibody for the other 2 h at room temperature. DAPI staining for another 10 min and the signal of fluorescence was observed by CLSM.

Cell cytotoxicity assay

Cell cytotoxicity test was assessed by Cell Counting Kit-8 assay. Briefly, tumor cells were seeded into the 96 well plates with 10^5 cells per well. After 12 h, a free medium containing different concentrations of Dox or D@L-AS1411 was added to the cells for 24 h. The cell viability was detected by the CCK-8 kit assay.

Bio-distribution of D@L and D@L-AS1411

RENCA tumor-bearing mice model was established by left forelimb under the armpit subcutaneous inoculation with RENCA cells (10^7 per mouse). When the tumor size arrived at 80 mm^3, D@L or D@L-AS1411 were intravenously injected into the mice, respectively (5 mg/kg). The red fluorescence signal of Dox was obtained by a multi-mode optical live imaging system (IVIS Lumina XRMS Series III, PerkinElmer, USA) at various time points. These organizations are weighed and then ground in an EP tube, followed by the addition of the corresponding PBS solution based on the weight of the organization to ensure a final tissue concentration of 0.5 mg/ml. After overnight shaking, the supernatant is collected using a centrifuge (12,000*g*, 10 min). Finally, Dox was quantified by UV–Vis with an absorption wavelength of 480 nm.

D@L-AS1411 is administered into mice via tail vein injection (5 mg/kg). At predetermined time points, blood is collected through the retro-orbital sinus to EP tubes containing 4% sodium citrate and centrifuged at 4 ℃ to obtain the supernatant (12,000*g*, 10 min). Finally, Dox is quantified using UV–Vis spectroscopy with an absorption wavelength of 480 nm. The anti-tumor efficacy of D@L-AS1411.

RENCA tumor-bearing mice model was established by subcutaneous inoculation with RENCA cells. When the tumor size arrived at 80 mm^3, RENCA tumor-bearing mice were therapy with PBS, Dox, D@L and D@L-AS1411. The tumor volume and body weight of each mouse were monitored every 2 days for 14 days. All the mice were killed and tumor tissues were collected at day 14.

Evaluation of tumor apoptosis and proliferation in vivo

After 14 days of therapy, the tumor tissues were embedded in OCT and cut into 6 μm slices to analyze T cell infiltration and distribution. Then, the tumor slices were stained with FITC conjugate anti-mouse CD3, PE conjugate anti-mouse CD4 and FITC conjugate anti-mouse CD8 antibody for 12 h at 4 ℃. Finally, DAPI stained the slices for the other 10 min, and fluorescence images of tumor slices were obtained by CLSM.

Hematoxylin and eosin (H&E) staining were also performed for histopathological analysis. On the other hand, Tunel assay kit (Beyotime, Shanghai, China) was also used to stain tumor tissue slices and tumor apoptosis was analyzed by CLSM.

Biosafety evaluation of D@L-AS1411

Mice were killed to collect the blood and major organs after 14 days treatment. To evaluate the hepatorenal toxicity of D@L-AS1411, we detected the serum levels of aspartate aminotransferase (AST), alanine aminotransferase (ALT), serum creatinine (CRE), and urea nitrogen (BUN) by assay kits purchased from the Jian Cheng Bioengineering Institute (Nanjing, China). In addition, the major organs were collected, fixed with 4% neutral formalin, and embedded in paraffin, followed by staining with H&E for histological analysis.

Results and discussion

Preparation and characterization of D@L-AS1411

In this study, a classic Liposome formulation composed of soy lecithin, cholesterol, and AS1411-PEG$_{2000}$-DSPE was utilized at a mole ratio of 60:38.5:1.5 was used to prepare D@L-AS1411. First, Dox@LIPO (D@L) was obtained through a mixture of soy lecithin and cholesterol into trichloromethane, followed by the membrane hydration method to load Dox. Subsequently, AS1411-PEG$_{2000}$-DSPE was inserted into the D@L to effectively expose AS1411 to the exterior region of the D@L, thus enhancing the ability of D@L-AS1411 to bind to tumor cells. The morphology of D@L-AS1411 or LIPO-AS1411 was evaluated using transmission electron microscopy (Fig. 1A and S1) and a Mastersizer analyzer. The results indicated a decrease in the size of the liposomes from 96 ± 2 nm to 108 ± 1.6 nm (PDI: 0.201 ± 0.078) after the encapsulation of Dox (Fig. 1B). Furthermore, upon insertion of AS1411, there was no significant change observed in the size of D@L and D@L-AS1411. However, the zeta potential of D@L increased from -19.8 mv to -23.4 mv after the insertion of AS1411, possibly attributable to due to the electronegativity of AS1411 (Fig. 1C). Subsequent observation of the spherical nanoparticles under TEM revealed that the particle size was slightly smaller than that detected by DLSM, potentially caused by volume collapse attributed to sample water loss. To verify the successful loading of AS1411 and Dox onto the liposomes, respectively. UV–Vis test results are shown in Fig. 1D, displaying characteristic absorption peaks of AS1411 and
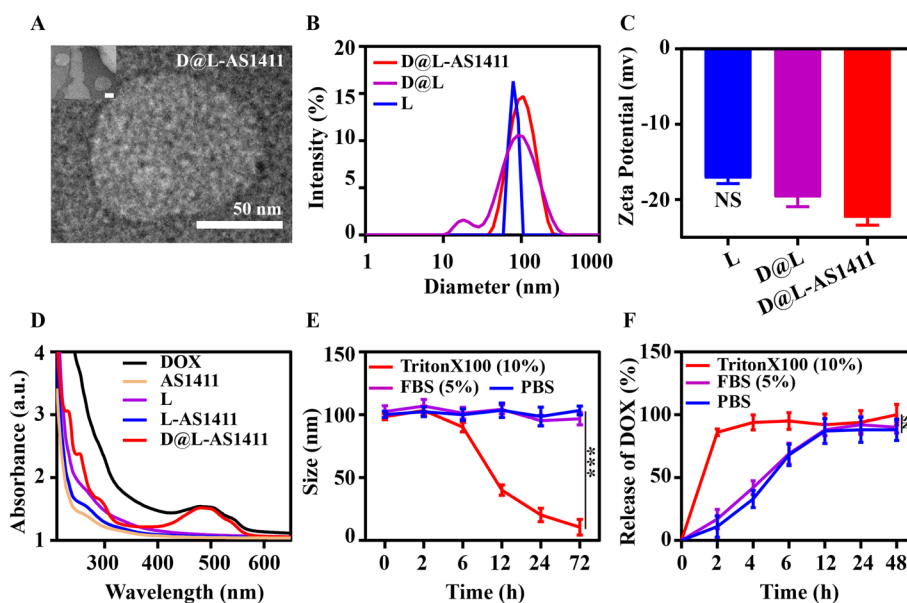
Fig. 1 Characterization of the D@L-AS1411. **A** Representative TEM image of the prepared D@L-AS1411, scale bar = 50 nm. **B** Hydrodynamic diameters of L, D@L, and D@L-AS1411. **C** Zeta potential of L, D@L, and D@L-AS1411 (*n* = 3). **D** UV–Vis spectra of Dox, AS1411, L, L-AS1411, and D@L-AS1411, respectively. **E** The stability of D@L-AS1411in PBS, Triton X-100, and FBS was detected by DLS (*n* = 3). **F** Release of Dox from D@L-AS1411 in PBS, FBS or Triton X-100 (*n* = 3). Statistical analysis was performed using two-tailed Student's *t* tests. ***$p < 0.001$. NS, no significant difference, $p > 0.05$

Dox at 260 nm and 480 nm, respectively, for D@L-AS1411. D@L-AS1411 were subsequently conducted under PBS, PBS solution containing 5% FBS (simulating blood), and a 10% Triton X-100 solution (a surfactant that can effectively disrupt liposome structure) to evaluate the stability, respectively. Analysis of the data presented in Fig. 1E, demonstrated that D@L-AS1411 was stable in serum and PBS solution, remaining stable for 72 h. The drug release behavior of D@L-AS1411 was also investigated (Fig. 1F), with results indicating a slow-release pattern, which is vital to avoid drug leakage within the body. Overall, these observations confirm the good stability of D@L-AS1411 and provide a guarantee for future in vivo experiments.

D@L-AS1411 enhances cellular uptake in vitro

AS1411 is a 24 bp nucleotide sequence that can bind to nucleolin protein, which expression on the surface of tumor cells such as MCF-7, RENCA, and HeLa (Wan et al. 2018; Yazdian-Robati et al. 2020). AS1411 is modified on the surface of the liposome to enhance the targeting efficacy in vivo. First, we detected the expression of nucleolin in RENCA cells, and the results are shown in Figure S2. The RENCA cells expressing nucleolin were used for subsequent experiments. To investigate the tumor-targeting capability of D@L-AS1411, a cellular uptake assay was determined by CLSM. RENCA cells were cultured in a 12 mm glass plate and pretreated with various concentrations of free AS1411 to saturate the available nucleolin binding sites on the cell surface. After 2 h incubation, the cells were incubated with D@L-AS1411 at the same concentration for another 4 h. Figure 2A, B shows that red fluorescence signals of Dox within the cytoplasm of all treated groups were obtained. Indicating the D@L-AS1411 was effectively
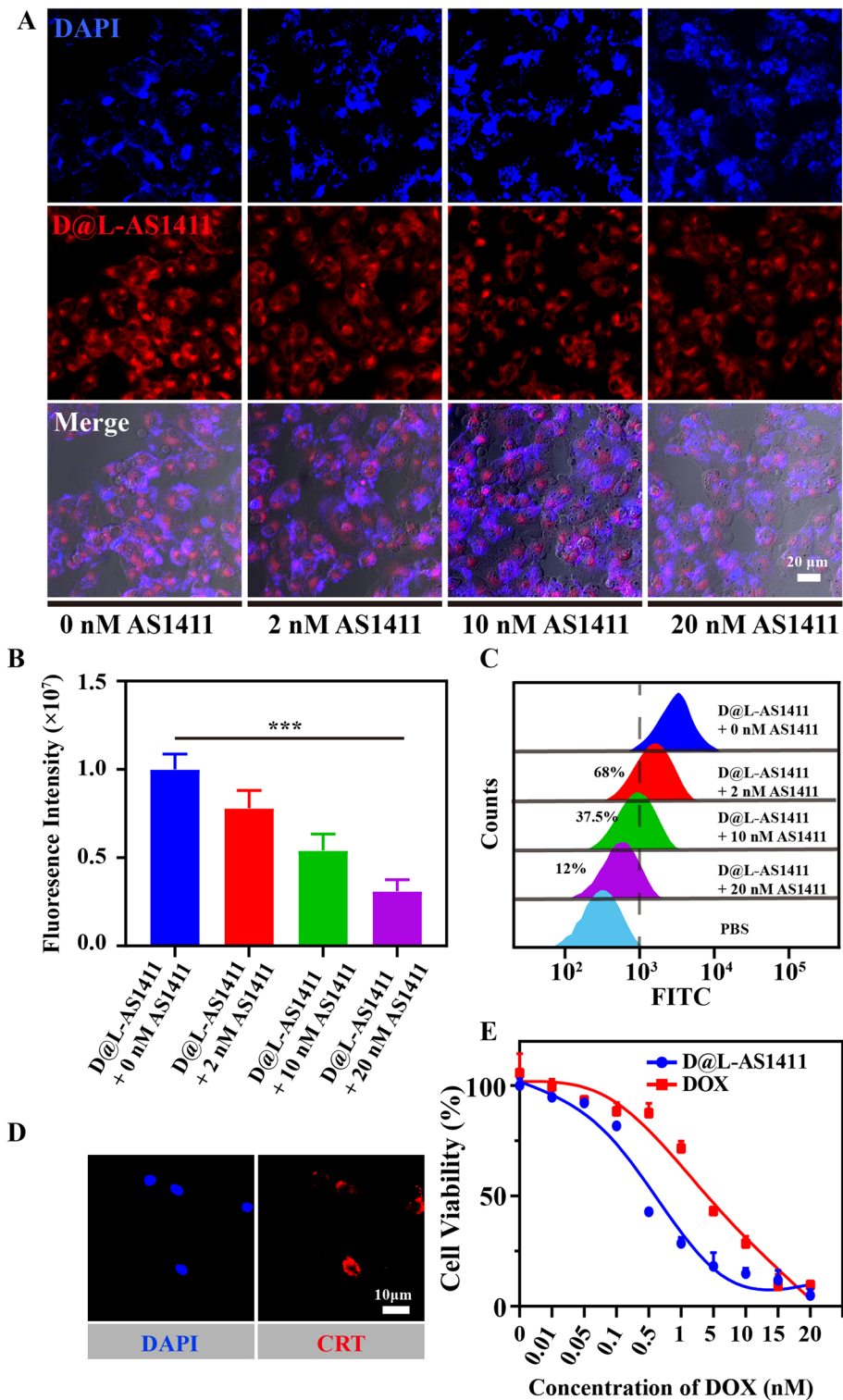
Fig. 2 D@L-AS1411 enhances the efficacy of Dox and induce ICD in vitro. **A** Representative fluorescence image of D@L-AS1411 uptake by RENCA cells, scale bar = 20 μm. **B** Fluorescence intensity of RENCA cells with various treatment (*n* = 3). **C** Flow cytometry of RENCA cells with various treatment. **D** Representative immunofluorescence images of D@L-AS1411-mediated CRT exposure, scale bar = 10 μm. **E** Cell viability of RENCA cells detected by CCK-8 assay (*n* = 3). Data were demonstrated as mean ± SD. Statistical analysis was performed via the two-tail Student's *t* test. ***$p < 0.001$

uptake by RENCA cells. Interestingly, the fluorescence intensity of the D@L-AS1411 plus 0 nM AS1411 group was higher than that of other treatment groups. As the concentration of free AS1411 increased, the red fluorescence intensity gradually diminished in the cytoplasm. At a free AS1411 concentration of 20 nM, the weakest red fluorescence signal was observed, suggesting that the uptake efficiency of D@L-AS1411 was hindered due to the occupation of nucleolin binding sites on the cell surface by free AS411. These data indicate the specific binding ability of D@L-AS1411 to nucleolin receptors on tumor cell surfaces to enhance drug uptake efficiency.

Flow cytometric analysis also obtained similar results (Fig. 2C). Compared with other groups, the group of therapy by D@L-AS1411 plus 20 nM free AS1411 exhibited a weak proportion of positive cells, just 12%, because the occupation of nucleolin binding sites on the cell surface by free AS411 inhibits cell uptake. These data further confirm the specific target of tumor cells by AS1411.

D@L-AS1411 induces RENCA immunogenic cell death in vitro

Calreticulin (CRT) is a crucial immunogenic death biomarker for recruiting immune cell infiltration and triggering an immunogenic anti-tumor response (Mu et al. 2023). Afterward, CLSM was employed to assess the expression of CRT after treatment with D@L-AS1411. The images demonstrated red fluorescence signals of CRT protein distributed on the cell surface (Fig. 2D) implying that D@L-AS1411 effectively induces immunogenic cell death in RENCA cells to elicit an immune-mediated anti-tumor response.

Finally, the therapeutic efficacy of D@L-AS1411 was assessed using the CCK-8 assay. As Fig. 2E shows, Dox and D@L-AS1411 exhibited concentration-dependent cell toxicity on RENCA tumor cells. However, compared to free Dox, D@L-AS1411 displayed a lower half inhibitory concentration (IC_{50}) value of 0.62 nM. This low IC_{50} value can be attributed to the enhanced uptake efficiency of tumor cells mediated by AS1411. Consequently, at the same drug concentration, a higher amount of Dox is uptake by RENCA tumor cells after 24 h of treatment, thereby enhancing the anti-tumor effect.

Pharmacokinetics and bio-distribution of D@L-AS1411

To evaluate the pharmacokinetics of D@L-AS1411, an in vivo real-time fluorescence imaging analysis system was utilized in mice with RENCA tumors. Following administration of D@L-AS1411 or D@L, the bio-distribution of Dox in the tumor significantly increased over time. As shown in Fig. 3A, B, at 24 h, and 48 h, a higher intensity of Dox red fluorescence signal was observed at the tumor sites compared to major organs such as the heart, liver, and kidney, indicating potential enhanced permeability and retention (EPR) effect, but the fluorescence intensity in the D@L treatment group showed a trend of gradual increase from 24 to 48 h, and at 48 h post-treatment, the fluorescence of D@L-AS1411 exhibited a mild enhancement of approximately twofold compared to the D@L treatment group. However, at the 72 h time point, no further fluorescence signal was detected in the D@L-treated group, contrasting with the sustained fluorescence observed in the D@L-AS1411 group, which can be attributed to the enhanced permeability and retention effect as well as the active tumor-targeting ability of AS1411. The concentration of Dox in the blood was also measured and presented in Fig. 3C, demonstrating that both D@L and D@L-AS1411 exhibited
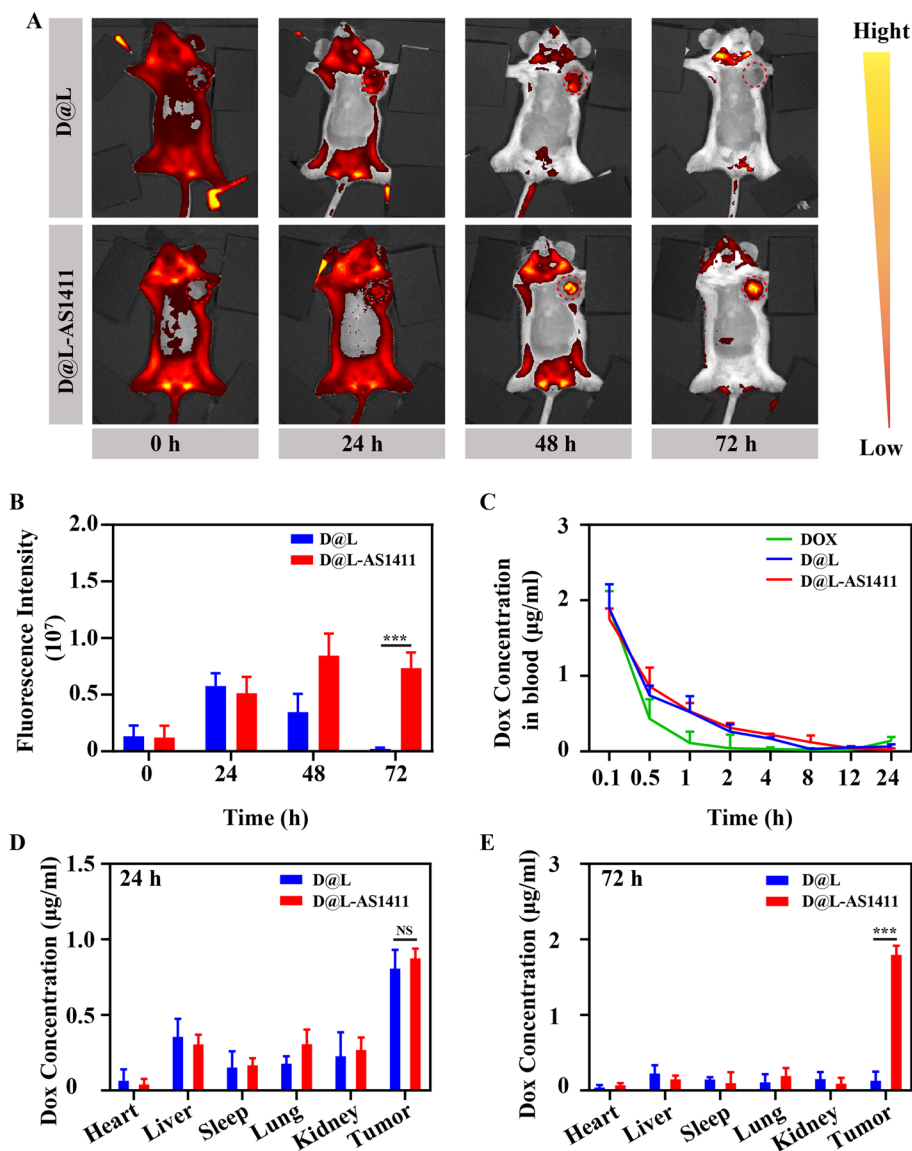
Fig. 3 Pharmacokinetics and bio-distribution of D@L-AS1411 in vivo. **A** The biodistances of D@L-AS1411 or D@L by real-time living image system. **B** Quantification of Dox fluorescence signal in the tumor tissues at various time points after indicated treatments. **C** Plasma concentration of Dox after indicated treatments at different time points. **D**, **E** Quantification of Dox concentration in tumors, and normal tissues at various times after D@L-AS1411 treatments ($n = 3$). Data were demonstrated as mean ± SD. Statistical analysis was performed via the two-tail Student's *t* test. ***$p < 0.001$; *NS* no significant difference, $p > 0.05$

extended blood circulation time, leading to enhanced Dox concentration in the tumor sites. Furthermore, the exact concentration of Dox in the tumor and major organs was determined using UV–Vis analysis (Fig. 3D, E), revealing approximately eight-fold higher accumulation of Dox in the tumors at 48 h after treatment with D@L or D@L-AS1411 compared to normal tissues like the heart, lung, and kidney. These results collectively indicate that D@L-AS1411 exhibits improved accumulation at the tumor site due to its longer blood circulation time and the tumor-targeting ability of AS1411.

In vivo anti-tumor efficacy of D@L-AS1411

To further evaluate the anti-tumor effect in vivo, a mouse tumor model burdened with RENCA tumor was constructed to validate the anti-tumor effect of D@L-AS1411. As shown in Fig. 4A, the growth rate of tumor volume in mice treated with D@L and D@L-AS1411 was significantly lower than that in other treatment groups based on the Dox-mediated tumor suppression effect. Meanwhile, the D@L-AS1411 treatment group almost completely inhibited tumor growth, while the tumor volume in the D@L treatment group was three times that of the D@L-AS1411 treatment group after 14 days of treatment. This indicates that AS1411 can target tumor cells in vivo. After 14 days of treatment, the mice were killed and the tumor tissues were removed surgically for weighing. As shown in Fig. 4B, the average weight of the tumor tissue after PBS treatment was
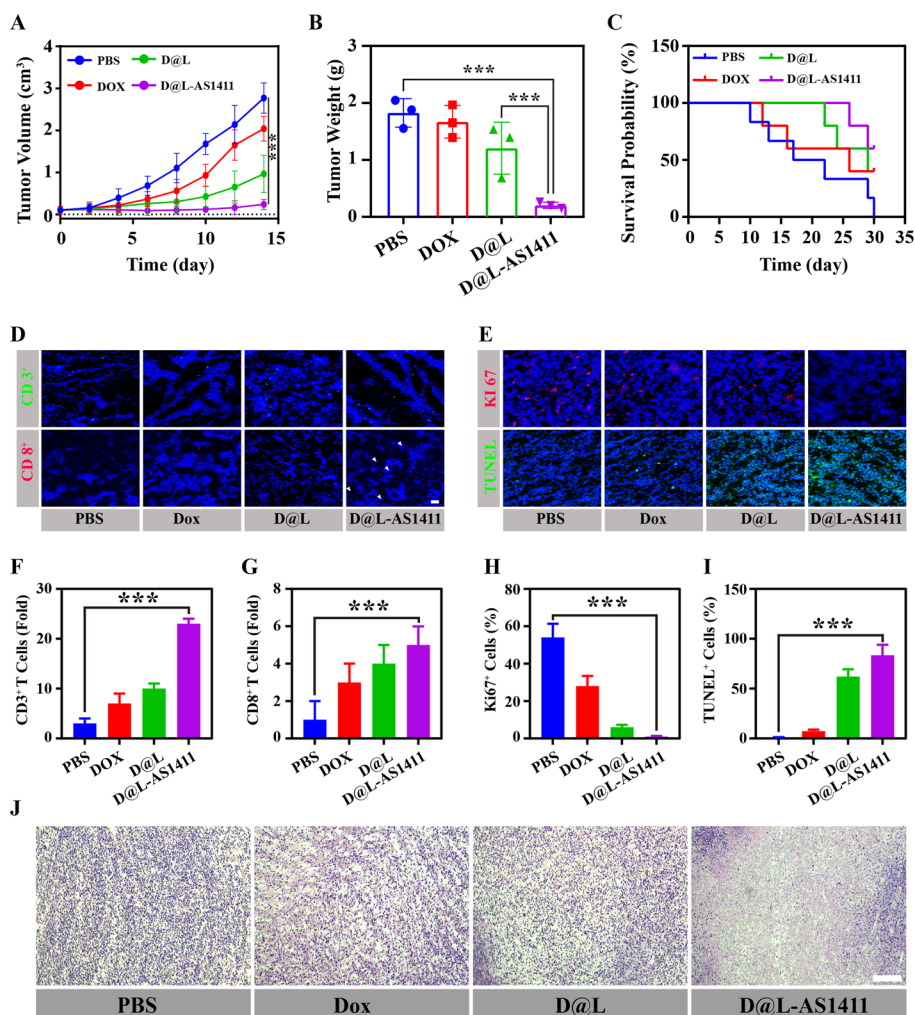

Fig. 4 In vivo anti-tumor effect of D@L-AS1411 and induce T cell infiltration. **A** Tumor growth curves of RENCA tumor-bearing mice after various treatments ($n = 4$). **B** Weight of collected RENCA tumors on Day 14 ($n = 3$). **C** The survival rate of RENCA tumor-bearing mice ($n = 4$). **D** Representative fluorescence images of CD3+ T cells, and CD8+ T cells, in RENCA tumor slices after treat 14 days, scale bar = 100 μm. **E** Representative images of Ki67 staining, and TUNEL staining, scale bar = 100 μm. **F–I** Quantification of CD3+, CD8+, TUNEL+ and Ki67+ in tumor cells slices. **J** Representative images of H&E staining, scale bar = 100 μm. Data were demonstrated as mean ± SD. Statistical analysis was performed via the two-tail Student's *t* test. ***$p < 0.001$

1.9 g, while the average weight of tumor after D@L-AS1411 treatment was only 0.3 g, showing a ninefold difference. In addition, the tumor mass in the D@L treatment group was also three times that of the D@L-AS1411 group, indicating the good tumor suppression effect and tumor-targeting ability of D@L-AS1411 through AS1411. Furthermore, there was a decreasing trend in the body weight of the mice during the 14-day treatment, which may be due to the influence of tumor growth on the normal food intake of the mice, leading to weight loss.

Then, we recorded the survival period of the mice after different drug treatments. As shown in Fig. 4C, after PBS treatment, the mouse tumors grew rapidly and all died within 30 days of treatment. Compared to other treatment groups, the mice treated with D@L-AS1411 had a prolonged survival period, with 60% of the mice still alive in the following 30 days.

D@L-AS1411 enhances the Dox accumulation at the tumor site. As shown in Figures S3 and S4, the red fluorescence intensity was stronger than the other treatment groups after the D@L-AS1411 treatment. Dox possesses the ability to induce immunogenic cell death (ICD) in tumor cells, leading to the release of molecular patterns that are associated with immune activation to facilitate the recruitment and infiltration of immune cells into the tumor microenvironment. The recruitment and infiltration of immune cells were evaluated at the tumor site by CLSM. The tumor cell slices were stained with FITC-anti-CD3 and PE-anti-CD8 antibodies. As shown in Fig. 4D, F, G, compared to the other groups, D@L-AS1411 exhibited intense green and red fluorescence signals at tumor slices. The results demonstrated an augmentation in the presence of CD3 and CD8-positive T lymphocytes within RENCA tumor tissue after treatment with D@L-AS1411. Thus, D@L-AS1411 also possessed the most obvious anti-tumor effect because AS1411 targets tumors and enhances the concentration of Dox at the tumor microenvironment in vivo.

After 14 days of treatment, the slices were stained with Ki67 and TUNEL to observe the proliferation and apoptosis of tumor cells. The results are shown in Fig. 4E, H, I. Compared to other treatment groups, after D@L-AS1411 treatment, the red fluorescence intensity decreased, indicating the inhibition of tumor cell growth. TUNEL and H&E staining (Figs. 4J and S5) consistently showed similar results, suggesting that D@L-AS1411 can effectively inhibit the growth of tumor cells.

Biocompatibility of D@L-AS1411 in vivo

The safety of D@L-AS1411 was tested by monitoring the live function, renal function, and H&E staining of the main organs of mice after 14 days of therapy. The liver function biomarkers, which ALT, and AST were detected by a liver function kit. As Fig. 5A–D shows, there was no significant difference between PSB and D@L-AS1411 therapy. Renal function tests also gave similar results, which indicate D@L-AS1411 also did not induce any toxicity to the renal function. Besides, H&E stains were further determined (Fig. 5E), compared with PBS-treated mice, D@L-AS1411 also caused no side effects to normal tissues (heart, liver, sleep, lungs, and kidneys), and in the mice there was no significant difference in body weight after 14 days treatment (Figure S6). These data show that D@L-AS1411 possessed no long-term significant toxicity in normal tissues. All these results above indicated that D@L-AS1411 with ideal biological safety in vivo.

In recent years, the development of nanomedicine delivery strategies has provided a solution to the toxic side effects of small molecule chemotherapy drugs (Chen et al. 2022). Liposomes, as one of the commonly used drug delivery carriers, can encapsulate drugs within a hydrophobic bilayer and a hydrophilic core (Juárez-Osornio and Gracia-Fadrique 2017). The size of liposomes, typically ranging from 50 to 100 nm, enables their accumulation at tumor sites through the enhanced permeability and retention (EPR) effect. However, the capture of liposomes by the liver often leads to a relatively low overall drug utilization rate.

To address this issue, we prepared D@L-AS1411 nanoparticles. By post-inserting PEG, AS1411 was anchored on the surface of D@L, forming a uniform and stable spherical structure. Furthermore, D@L-AS1411 efficiently releases Dox (Fig. 1). Notably, D@L-AS1411 can be effectively taken up by RENCA cells and induce immunogenic cell death (Fig. 2), thereby recruiting immune cells to infiltrate the tumor site (Fig. 4). Additionally, in vivo imaging using a live imaging system confirmed the tumor-targeting ability of D@L-AS1411, demonstrating an increased accumulation of the drug at the tumor site (Fig. 3). Moreover, the mouse tumor model further demonstrated the effective inhibition of tumor cell growth by D@L-AS1411, leading to prolonged survival of the treated mice (Fig. 4). Furthermore, there was no apparent damage observed in the major organs of the mice after treatment (Fig. 5), which can be attributed to the tumor-targeting ability of AS1411.Overall, these results indicate that D@L-AS1411 can enhance the accumulation of drugs at the tumor site by targeting RENCA tumor cell surface nucleolin, thereby enhancing the anti-tumor efficacy.
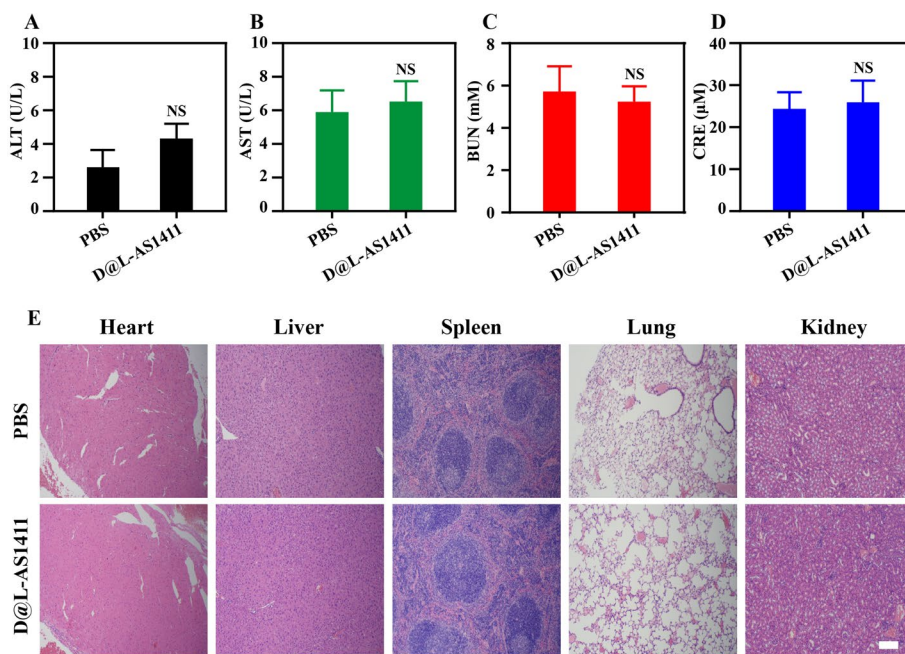

Fig. 5 Toxicity tests of D@L-AS1411 on Balb/C mice. **A–D** Serum biochemistry data of ALT, AST, CRE, and BUN reflecting the liver or kidney function (*n*=3). **E** H&E staining images of liver, heart, spleen, kidney, and lung on Day 14, scale bar=100 μm. Data were demonstrated as mean±SD. *ND* no significant difference

Conclusions

In this study, a tumor-targeting nanoplatform D@L-AS1411 was developed to enhance the accumulation of the chemotherapeutic drug Dox at the tumor site through a simple film hydration method. The tumor-targeting ability of AS1411 not only improved the tumor-targeting ability of D@L-AS1411 in vivo to increase the accumulation of Dox at the tumor site but also induced immunogenic cell death (ICD) in tumor cells, stimulating immune responses and enhancing the infiltration of CD3$^+$ and CD8$^+$ T lymphocytes at the tumor site. Therefore, the delivery platform based on Lipd-AS1411 significantly improved the anti-tumor effect of Dox. This nanodrug delivery platform is promising for clinical application based on its anti-tumor ability and good biocompatibility. In summary, this study not only provides an efficient tumor-targeting delivery platform but also contributes to the improvement of chemotherapy−immunotherapy combination for tumor treatment strategy in the clinic.

Statistical analysis

All the data were analyzed using GraphPad Prism 8.0.1. The results were analyzed using two-tailed Student's *t* tests. *$p < 0.05$ was regarded as statistically significant; **$p < 0.01$ and ***$p < 0.001$ were regarded as highly significant; NS represented no significant difference ($p > 0.05$).

Supplementary Information

The online version contains supplementary material available at https://doi.org/10.1186/s12645-024-00262-6.

> Supplementary Material 1.

Availability of data and materials
Data will be made available on request.

Declarations

Ethics approval and consent to participate
All the procedures strictly complied with the ethical and legal requirements of the Administration Committee of Experimental Animals in Suzhou Province and were approved by the First Affiliated Hospital of Soochow University.

Consent for publication
All the authors contributed to the article and approved the submitted version.

Competing interests
The authors declare no competing interests.

References

Al-Harbi NS, Alrashood ST, Siddiqi NJ, Arafah MM, Ekhzaimy A, Khan HA (2020) Effect of naked and PEG-coated gold nanoparticles on histopathology and cytokines expression in rat liver and kidneys. Nanomedicine 15(3):289–302

Bing C, Patel P, Staruch RM, Shaikh S, Nofiele J, Wodzak Staruch M, Szczepanski D, Williams NS, Laetsch T, Chopra R (2018) Longer heating duration increases localized doxorubicin deposition and therapeutic index in Vx2 tumors using MR-HIFU mild hyperthermia and thermosensitive liposomal doxorubicin. Int J Hyperthermia 36(1):195–202

Chen GY, Li DH, Jin Y, Zhang WY, Teng LR, Bunt C, Wen JY (2014) Deformable liposomes by reverse-phase evaporation method for an enhanced skin delivery of (+)-catechin. Drug Dev Ind Pharm 40(2):260–265

Chen C, Zhou Y, Chen C, Zhu S, Yan X (2022) Quantification of available ligand density on the surface of targeted liposomal nanomedicines at the single-particle level. ACS Nano 16(4):6886–6897

Fu XD, Lu YY, Guo JP, Liu H, Deng AP, Kuang CC, Xie XY (2019) K237-modified thermosensitive liposome enhanced the delivery efficiency and cytotoxicity of paclitaxel. J Liposome Res 29(1):86–93

Ibrahim MM, Tawfique SAH, Mahdy MM (2014) Liposomal diltiazem HCl as ocular drug delivery system for glaucoma. Drug Dev Ind Pharm 40(6):765–773

Imranul-haq M, Hamilton JL, Lai BFL, Shenoi RA, Horte S, Constantinescu I, Leitch HA, Kizhakkedathu JN (2013) Design of long circulating nontoxic dendritic polymers for the removal of iron in vivo. ACS Nano 7(12):10704–10716

Jiang LY, Wang H, Chen SZ (2020) Aptamer (AS1411)-conjugated liposome for enhanced therapeutic efficacy of miRNA-29b in ovarian cancer. J Nanosci Nanotechnol 20(4):2025–2031

Jiang Q, Yao F, An Y, Lai X, Li X, Yu Z, Yang X-D (2024) Novel nanotherapeutics for cancer immunotherapy by albumin nanoparticles functionalized with PD-1 and PD-L1 aptamers. Cancer Nanotechnol 15(1):3

Juárez-Osornio C, Gracia-Fadrique J (2017) Structures similar to lipid emulsions and liposomes. Dipalmitoylphosphatidylcholine, cholesterol, Tween 20-Span 20 or Tween 80-Span 80 in aqueous media. J Liposome Res 27(2):139–150

Kalyanaraman B, Cheng G, Zielonka J, Bennett B (2019) Low-temperature EPR spectroscopy as a probe-free technique for monitoring oxidants formed in tumor cells and tissues: implications in drug resistance and OXPHOS-targeted therapies. Cell Biochem Biophys 77(1):89–98

Kong T, Zhou R, Zhang Y, Hao L, Cai X, Zhu B (2019) AS1411 aptamer modified carbon dots via polyethylenimine-assisted strategy for efficient targeted cancer cell imaging. Cell Prolif 53(1):e12713

Law LW (1956) Differences between cancers in terms of evolution of drug resistance. Cancer Res 16(7):698–716

Li S, Zhang Y, Ho SH, Li B, Wang M, Deng X, Yang N, Liu G, Lu Z, Xu J, Shi Q, Han JY, Zhang L, Wu Y, Zhao Y, Nie G (2020) Combination of tumour-infarction therapy and chemotherapy via the co-delivery of doxorubicin and thrombin encapsulated in tumour-targeted nanoparticles. Nat Biomed Eng 4(7):732–742

Liu X, Wang Q, Zhao HH, Zhang LC, Su YY, Lv Y (2012) BSA-templated MnO_2 nanoparticles as both peroxidase and oxidase mimics. Analyst 137(19):4552–4558

Liu G, Zhao X, Zhang Y, Xu J, Xu J, Li Y, Min H, Shi J, Zhao Y, Wei J, Wang J, Nie G (2019) Engineering biomimetic platesomes for pH-responsive drug delivery and enhanced antitumor activity. Adv Mater 31(32):e1900795

Lokova AY, Zaborova OV (2019) Modification of fliposomes with a polycation can enhance the control of pH-induced release. Int J Nanomed 14:1039–1049

Mu YT, Fan YX, He LP, Hu NN, Xue H, Guan XG, Zheng ZJ (2023) Enhanced cancer immunotherapy through synergistic ferroptosis and immune checkpoint blockade using cell membrane-coated nanoparticles. Cancer Nanotechnol 14(1):83

Pavitra E, Dariya B, Srivani G, Kang SM, Alam A, Sudhir PR, Kamal MA, Raju GSR, Han YK, Lakkakula BVKS, Nagaraju GP, Huh YS (2021) Engineered nanoparticles for imaging and drug delivery in colorectal cancer. Semin Cancer Biol 69:293–306

Pesarrodona M, Sánchez-García L, Seras-Franzoso J, Sánchez-Chardi A, Baltá-Foix R, Cámara-Sánchez P, Gener P, Jara JJ, Pulido D, Serna N, Schwartz S, Royo M, Villaverde A, Abasolo I, Vazquez E (2020) Engineering a nanostructured nucleolin-binding peptide for intracellular drug delivery in triple-negative breast cancer stem cells. ACS Appl Mater Interfaces 12(5):5381–5388

Si L, Yang S, Lin R, Gu S, Yan C, Yan J (2024) SiO_2–alginate–melittin nano-conjugates suppress the proliferation of ovarian cancer cells: a controlled release approach leveraging alginate lyase. Cancer Nanotechnol 15(1):4

Sugarbaker PH, Stuart OA (2021) Pharmacokinetics of the intraperitoneal nanoparticle pegylated liposomal doxorubicin in patients with peritoneal metastases. EJSO 47(1):108–114

Wan Y, Wang L, Zhu C, Zheng Q, Wang G, Tong J, Fang Y, Xia Y, Cheng G, He X, Zheng SY (2018) Aptamer-conjugated extracellular nanovesicles for targeted drug delivery. Cancer Res 78(3):798–808

Wang J, Xiao W, Teng H, Yin H, Chen X, Jiang X, Huo C, Teng M, Ma S, Al-Haimi AANM (2018) Cu_2O/hollow mesoporous silica composites for the rapid and efficient removal of methylene blue. Environ Technol 41(17):2157–2164

Wang C, Xu J, Zhang Y, Nie G (2023) Emerging nanotechnological approaches to regulating tumor vasculature for cancer therapy. J Control Release 362:647–666

Wendler F, Purice TM, Simon T, Stebbing J, Giamas G (2021) The LMTK-family of kinases: emerging important players in cell physiology and pathogenesis. Biochim Biophys Acta 1867(9):165372

Xiong W, Qi L, Jiang N, Zhao Q, Chen L, Jiang X, Li Y, Zhou Z, Shen J (2021) Metformin liposome-mediated PD-L1 downregulation for amplifying the photodynamic immunotherapy efficacy. ACS Appl Mater Interfaces 13(7):8026–8041

Xu J, Wan K, Wang H, Shi X, Wang J, Zhong Y, Gao C, Zhang Y, Nie G (2021) Polyethylenimine-poly(lactic-*co*-glycolic acid) (2) nanoparticles show an innate targeting ability to the submandibular salivary gland via the muscarinic 3 receptor. ACS Cent Sci 7(11):1938–1948

Yang DD, Nguyen PL (2021) Optimizing androgen deprivation therapy with radiation therapy for aggressive localized and locally advanced prostate cancer. Urol Oncol 39(10):720–727

Yazdian-Robati R, Bayat P, Oroojalian F, Zargari M, Ramezani M, Taghdisi SM, Abnous K (2020) Therapeutic applications of AS1411 aptamer, an update review. Int J Biol Macromol 155:1420–1431

Zhang N, Wu X, Xu W, Chen L, Tu X (2023) Fourth-line targeted drugs for the long-term treatment of patients with secondary gastrointestinal stromal tumors with multisite mutations: a case report. Ann Palliat Med 12(1):227–235

Publisher's Note

Springer Nature remains neutral with regard to jurisdictional claims in published maps and institutional affiliations.